ARTICLE

Check for updates

In-gap band formation in a periodically driven charge density wave insulator

Alexander Osterkorn [1,2✉], Constantin Meyer[1] & Salvatore R. Manmana [1✉]

Modern time-resolved spectroscopy experiments on quantum materials raise the question, how strong electron-electron interactions, in combination with periodic driving, form unconventional transient states. Here we show using numerically exact methods that in a driven strongly interacting charge-density-wave insulator a band-like resonance in the gap region is formed. We associate this feature to the so-called Villain mode in quantum-magnetic materials, which originates in moving domain walls induced by the interaction. We do not obtain the in-gap band when driving a non-interacting charge density wave model. In contrast, it appears in the interacting system also in equilibrium at intermediate temperatures and in the short-time evolution of the system after a quantum quench to the lowest-order high-frequency effective Floquet Hamiltonian. Our findings connect the phenomenology of a periodically driven strongly correlated system and its quench dynamics to the finite-temperature dynamical response of quantum-magnetic materials and will be insightful for future investigations of strongly correlated materials in pump-probe setups.

[1] Institute for Theoretical Physics, Georg-August-University Göttingen, Friedrich-Hund-Platz 1, D-37077 Göttingen, Germany. [2] Jožef Stefan Institute, Jamova 39, SI-1000 Ljubljana, Slovenia. ✉email: osterkorn@theorie.physik.uni-goettingen.de; salvatore.manmana@uni-goettingen.de

A central driving force of modern condensed matter physics is the realization of novel phases of matter out-of-equilibrium like transient superconductivity[1–5] or excitonic insulators in transition metal dichalcogenides (TMDCs)[6–12]. These are typically created from a highly complex interplay of band structure, (electronic) interactions, and excitations by a light-field. Nowadays, experimental techniques allow to actively "engineer" properties of many-body quantum systems in such out-of-equilibrium systems in a highly controlled way[13–15]. This opens up the possibility to create behavior that is not even possible in equilibrium setups. An important pathway is to induce excitations whose interplay with the electronic interactions can lead to intriguing transient behavior. Such excitations can be realized in experiments, e.g., by ultrashort laser pulses in so-called pump-probe setups[16–19], or by continuous periodic driving of the systems, e.g., by shaking ultracold atom systems on optical lattices[20–26]. A much studied theoretical idealization is (infinite) periodic driving, which can be addressed by Floquet theory. In this framework and within certain limits, the properties of the system can be described by a time-independent effective Hamiltonian[27,28]. Control over the parameters of the driving translates to control over the effective Hamiltonian and this, in turn, allows to manipulate order parameters[29], induce topological order[30] etc.

It is possible to derive time-independent approximate effective Hamiltonians in the low-[31] and high-frequency[27,32] regimes, and development of methods in this vein is ongoing[33]. In addition, the periodic driving generically leads to energy absorption evolving the system towards an infinite-temperature state[34,35]. This restricts the relevance of such effective Hamiltonians to regimes in which the energy absorption is suppressed—like the high-frequency regime. Additional transient dynamics can be induced by the switching-on procedure[28,36–39]. One major topic of interest is the role of interactions in strongly driven systems. It has been shown that in Hubbard systems at resonance the interaction can be renormalized, and double occupancies can be enabled[27,32,40]; one can even tune the parameters of the driving so that the fermions behave like free particles[41]. In experiments on topological insulators, the formation of Floquet side-bands has been reported[42,43] in time-resolved angle-resolved photoemission (ARPES) spectra. For strongly correlated systems, however, their experimental observation and theoretical understanding are still open questions[44–46], and it is interesting to search for additional interaction-induced effects in nonequilibrium spectra.

In our work, we investigate periodically driven strongly interacting fermions after a sudden switching-on of the drive and without assuming the high-frequency approximation. We shed light on the effect of interactions on the transient dynamics, and we find the formation of a cosine-like band inside the gap-region of the spectral function, even though in the ground state single particle excitations have no support in this region. This is reminiscent of the creation or excitation of quasiparticles[47] and their dispersion in the transient state before thermalization. To this end, we calculate non-equilibrium spectral functions with unbiased matrix product state (MPS)[48,49] approaches, and systematically investigate correlation effects by comparing to non-interacting and mean-field scenarios. This is in contrast to other approaches, which e.g. rely on the Floquet-Magnus expansion[27,41] in terms of the inverse driving frequency. We focus on a simple paradigmatic model for strongly correlated physics, namely a chain of spinless fermions with nearest-neighbor interactions. At half filling and zero temperature the model is known to undergo a Berezhinskii-Kosterlitz-Thouless (BKT) type transition[50] from a Luttinger liquid (LL)[51] to an interacting charge density wave (CDW) insulator[52] when increasing the interaction strength. Driving the system with frequencies much larger than the gap

("Magnus case"), a renormalization of the gap size for this system is predicted[29].

As periodic driving heats up the system, we compare our nonequilibrium results to spectral functions at finite temperatures. There, it is known from the structure factors of quantum magnets that at finite temperatures features in the gap region can be realized (e.g., the so-called "Villain mode"[53–56], scattering of magnons[57], or bound states[58]). Here, we will discuss the behavior of the periodically driven fermionic system in light of these findings.

Results

Model. We consider a periodically driven chain of interacting spinless fermions described by the Hamiltonian

$$\hat{H}(t) = -t_h \sum_{l=1}^{L-1} \left(e^{iA(t)} c_l^\dagger c_{l+1} + \text{H.c.} \right)$$
$$+ V \sum_{l=1}^{L-1} \left(n_l - \frac{1}{2} \right) \left(n_{l+1} - \frac{1}{2} \right) \quad (1)$$
$$+ \sum_{l=1}^{L} \mu_l n_l,$$

where V is the strength of the density-density interaction and μ_l is an additional, l-dependent on-site potential (e.g., a pinning field at the edge), which in the numerical calculations allows us to select one of the symmetry-broken CDW states, see the Methods section. $A(t) = \theta(t) A_0 \sin(\Omega t)$ is a time-dependent vector potential, which is switched on at time $t = 0$. This approach is known as Peierls substitution[59] and models a classical light field, which couples to the electrons in the system (here: spinless fermions). At equilibrium, this model can be mapped to a spin-1/2 XXZ quantum magnet via Jordan-Wigner transform. We will mostly consider open boundary conditions (OBC) and for comparison periodic boundary conditions (PBC). For $A(t) \equiv 0$, Bethe ansatz (BA)[60] gives the BKT transition at $V/t_h = 2$. In the following, we will drive a system starting in the temperature $T = 0$ CDW ground state at $V/t_h = 5$, for which the energy gap according to BA[60] is $\Delta/t_h \approx 1.576$.

We define the non-equilibrium generalization of the spectral function via the Fourier transform of the retarded Green's function

$$A_k^{\text{ret}}(t, \omega) = -\text{Im} \frac{1}{\sqrt{2\pi}} \int_{-\infty}^{\infty} d\tau \, e^{(i\omega - \eta)\tau} G_{kk}^{\text{ret}}(t, \tau),$$
$$G_{\alpha\beta}^{\text{ret}}(t', \tau) := -i\theta(\tau) \left\langle \left\{ c_\alpha(t' + \tau), c_\beta^\dagger(t') \right\} \right\rangle \quad (2)$$

with a damping factor $\eta \approx 0.1$ as further explained in the Methods section. As discussed there, t is the waiting time after turning on the periodic drive (note that waiting time $t = 0$ is not the same as equilibrium, since these are the results immediately after turning on the driving, and the time evolution over τ is performed with the driven, time-dependent Hamiltonian). This quantity relates to measurements in time-dependent angle-resolved photoemission spectroscopy (trARPES), although a more detailed modelling is required for a direct comparison to experiments[17,61,62], as well as for its interpretation in the deep nonequilibrium regime[63]. Integration of $A_k^{\text{ret}}(t, \omega)$ over the crystal momenta k directly yields the time-dependent density of states (tDOS). These quantities allow us to study qualitative changes of the spectral function with time, such as the formation of additional branches, or a change of the band structure due to the excitation.

We complement our study by considering the time evolution of the CDW order parameter

$$\mathcal{O}_{\text{CDW}}(t) := \frac{2}{L} \sum_{i \text{ even}} \left\langle n_{i+1}(t) - n_i(t) \right\rangle; \quad (3)$$
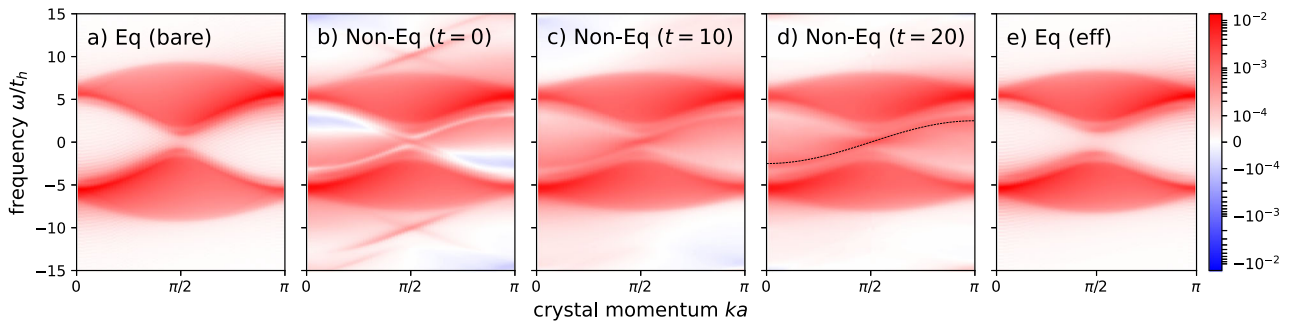
Fig. 1 (Non-)Equilibrium spectral functions of the periodically driven charge-density wave (CDW) state. The system is prepared initially in the ground state at interaction strength $V/t_h = 5$ and is driven with a periodic drive of frequency $\Omega/t_h = 10$. **a** Equilibrium spectral function $A_k^{\text{ret}}(\omega)$ of the system. **b**–**d** Non-equilibrium spectral functions $A_k^{\text{ret}}(t,\omega)$ upon driving at the instances indicated. Times are measured in units of the inverse hopping amplitude t_h^{-1}. **e** Equilibrium spectral function $A_k^{\text{ret}}(\omega)$ of the system with renormalized hopping parameter t_h^{eff}, for comparison. The spectral features in **e** are also present in the spectral function of the driven system (**b**–**d**). In addition, there is clearly additional spectral weight appearing out-of-equilibrium, whose main feature is well approximated by $f(k) \approx -2.5\cos(ka)$ (black line in **d**). All data is obtained with time evolution based on matrix product states for a chain with $L = 64$ lattice sites and open boundary conditions. The color scheme encodes the values of $A_k^{\text{ret}}(t,\omega)$, where blue represents negative and red positive values.
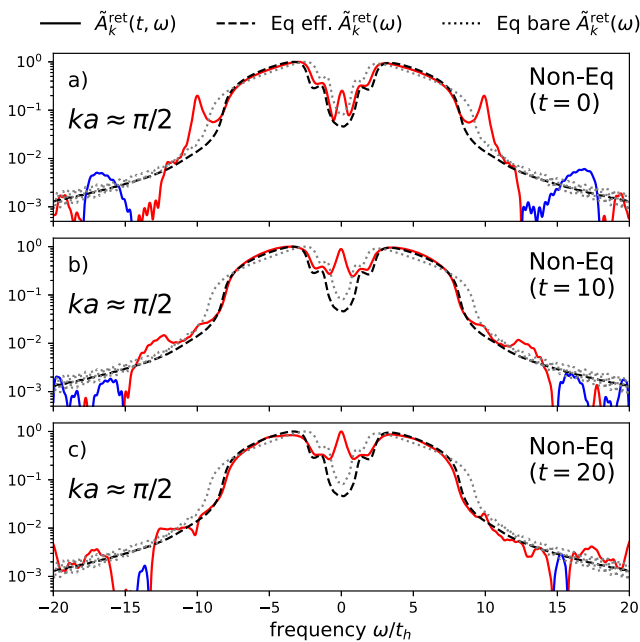

Fig. 2 Cross section plots through the data in Fig. 1 at electronic crystal momentum $k \approx \frac{\pi}{2}$. The spectral functions in the panels are obtained at times (**a**) $t = 0$, (**b**) $t = 10$ and (**c**) $t = 20$, respectively. Dotted grey lines: Rescaled equilibrium spectral function $\tilde{A}_k^{\text{ret}}(\omega)$ of the initial charge-density wave state without driving and for a hopping amplitude $t_h = 1$. Dashed black lines: analogous data for a renormalized hopping amplitude $t_h^{\text{eff}} \approx 0.7652 t_h$. Solid lines: Rescaled non-equilibrium spectral functions $\tilde{A}_k^{\text{ret}}(t,\omega)$ (red color = positive, blue color = negative). All data shown is rescaled such that the maximum value of the data at this k-slice is equal to one for better visual comparison of the spectral weight distribution, $\tilde{A}_k^{\text{ret}}(t,\omega) = A_k^{\text{ret}}(t,\omega) \, / \, \max_\omega A_k^{\text{ret}}(t,\omega)$.

further details are explained in the Methods section. We also keep track of the time evolution of the energy, $E(t) = \langle H(t)\rangle$, which serves as a measure for the heating of the system.

Driving a strongly correlated charge-density-wave insulator. For frequencies Ω well above the band gap ("Magnus case") the properties of the periodically driven model are expected to be well-described by an effective Hamiltonian according to the

Floquet-Magnus/high-frequency expansion[29,32]. It is given by the original Hamiltonian but with a renormalized hopping parameter[64] $t_h^{\text{eff}} = J_0(A_0)t_h \approx 0.7652 t_h$ for $A_0 = 1$. This corresponds to a model with $V/t_h^{\text{eff}} \simeq 1.3 V/t_h$. In the following, we consider these aspects by studying the system at $V/t_h = 5$, which is deep in the CDW insulating phase.

Figures 1 and 2 show results for the equilibrium and the non-equilibrium spectral functions at waiting times $t = 0$, $10t_h^{-1}$, and $20t_h^{-1}$. The driving frequency of $\Omega/t_h = 10 > \Delta/t_h \approx 1.576$ is larger than the spectral gap but not substantially larger than the interaction strength so that we are not deeply in the Magnus regime. Figure 1e shows the equilibrium spectral function for the effective Hamiltonian with the renormalized hopping matrix element. Let us consider the equilibrium results first: In Fig. 1a we can identify the equilibrium continuum of excitations[65] as well as the spectral gap located around $\omega = 0$. Despite finite size effects its minimal size around $k = \pi/2$ is in agreement with the BA prediction. The spectral function of the effective Hamiltonian in Fig. 1e looks similar to Fig. 1a but the width of the continuum is smaller and the gap is larger. Turning to the non-equilibrium results, we see that the spectral function at waiting time $t = 0$ in Fig. 1b looks quite similar to the equilibrium result for the effective Hamiltonian in Fig. 1e, but it possesses additional features. In particular, an in-gap band comes into appearance and the continuum changes slightly its size and form. Around frequencies $\omega/t_h = \pm 10$ weak signals appear, which seem to echo the in-gap feature. These are reminiscent of Floquet sidebands, which are observed in time-resolved ARPES experiments[42]. It is noteworthy, however, that one seems to obtain these "echoes" only for the in-gap signal, but not for the main spectral features. This needs further investigations, which go beyond the scope of the present paper. At later waiting times $t = 10t_h^{-1}$ in Fig. 1c and $t = 20t_h^{-1}$ in Fig. 1d, the shape of the continuum does not further change, but the in-gap signal becomes more pronounced. This is further confirmed by Fig. 2, which shows a momentum cut through the central region of the spectral function at $k \approx \pi/2$ for waiting times $t = 0$, $10t_h^{-1}$ and $20t_h^{-1}$. In order to better focus on the relative distribution of spectral weight we normalized all spectral functions to their maximum value at that k-slice. In all cases, we identify two main lobes and smaller peaks. Let us follow the behavior of the main lobes and of the largest peaks at $\omega = \pm 10$ and $\omega = 0$: At waiting time $t = 0$, the lobes show a small difference between the nonequilibrium result and the result of the
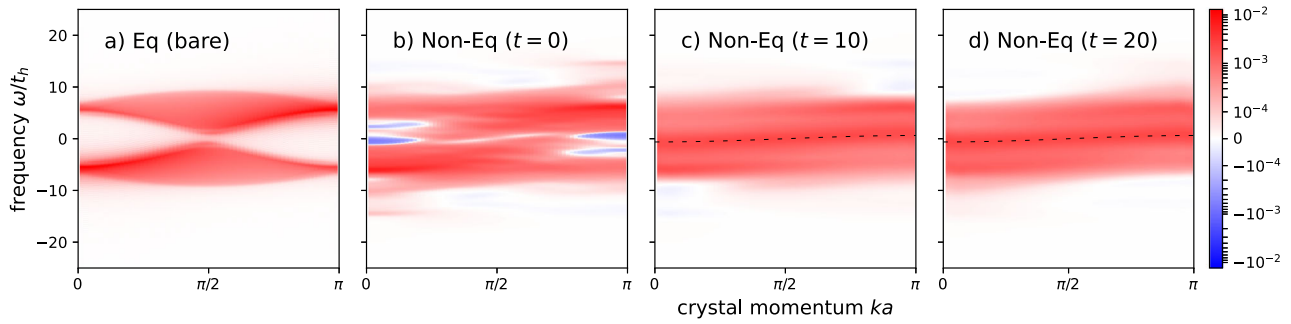
Fig. 3 Spectral functions of the periodically driven charge-density wave state with drive frequency $\Omega \approx 4.2 t_h$. The system is prepared initially in the ground state at interaction strength $V/t_h = 5$. **a** Equilibrium spectral function, **b–d** Nonequilibrium spectral functions $A_k^{\text{ret}}(t, \omega)$ of the driven system. The color scheme encodes the value of $A_k^{\text{ret}}(t, \omega)$, where blue represents negative and red positive values. The dotted lines in **c** and **d** show the function $f(k) \sim -\frac{2.5}{4}\cos(ka)$ as a guide to the eye (note the difference to the guiding line in Fig. 1). The data in this figure was obtained from time evolution with matrix product states (MPS) for a chain length of $L = 64$ sites and with open boundary conditions.

effective Hamiltonian, which becomes even smaller at later waiting times. It is noteworthy that the similarity to the effective description is already obtained at waiting time $t = 0$, although the effective Hamiltonian relied on the infinite-driving assumption. The additional signals at $\omega/t_h = \pm 10$ oscillate in time, but are suppressed with increasing time. Nevertheless, the peak at $\omega = 0$ becomes more pronounced with time and so the cosine-like in-gap feature of Fig. 1 appears stable on the time scales treated by us. We checked that it is also present for other system sizes and periodic boundary conditions (PBC) so that boundary effects can be ruled out as an explanation (cf. Supplementary Note 1). By comparing results for $L = 32$ and $L = 64$ we find that the peak gets sharper for larger system size, while keeping the relative weight. At early waiting times negative weight appears in the spectral function. This is not an artefact and traces back to the non-equilibrium nature of the state. It was reported recently[37,66] that upon averaging of the Wigner coordinate $t_{\text{ave}} = (t + t')/2$ over a driving period, the non-equilibrium density of states for fermions can be shown to be positive. However, at later waiting times away from the turning-on of the field at time $t = 0$, our spectral function (obtained using "horizontal time coordinates"[37]) is also almost completely positive without this procedure.

To better understand our findings, we study in Fig. 3 the system at the same value of $V/t_h = 5$ but with a driving frequency closer to resonance $\Omega/t_h \approx 42 \cdot 10^{-1}$ for comparison. The additional feature in the gap region in this case is even more strongly pronounced and it goes hand in hand with a significant reduction of the original spectral features of the CDW insulator. The question arises how this disappearance of the holon continuum is connected to a destruction of the CDW state. To study this, we calculate the CDW order parameter $\mathcal{O}_{\text{CDW}}(t)$, which is displayed in Fig. 4a for driving in the Magnus regime and closer to resonance. In the latter case, $\mathcal{O}_{\text{CDW}}(t)$ completely vanishes on a time scale $t \approx 10 t_h^{-1}$, which is in agreement with the time scale on which the holon continuum disappears in the spectral function. The behavior for $\Omega/t_h = 10$ is more complicated, but also here a partial reduction of the CDW order is realized, which continues over times longer than the ones treated by us. Note that the parameters of the effective Hamiltonian are deeper in the CDW phase such that in equilibrium one would expect a larger CDW order parameter. In contrast, here we observe a partial melting of the order, which is due to the absorption of energy. Driven systems in the long-time limit will realize an infinite-temperature state[34,35]. In our case, as can be seen in Fig. 4b, the energy continues to increase as a function of time indicating that, on the transient time scale treated by us, the
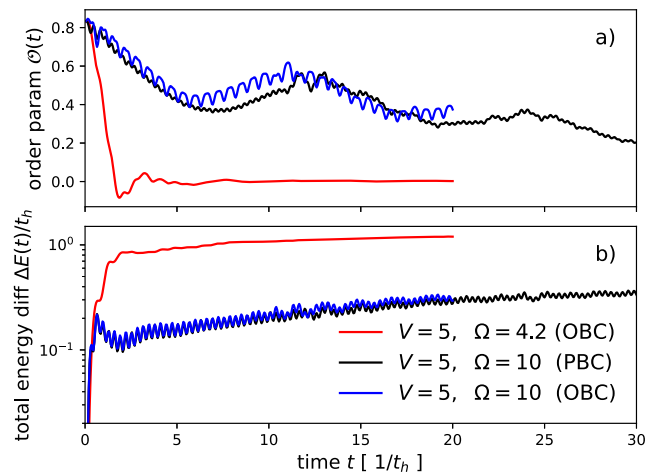

Fig. 4 Dynamics of the total energy change $\Delta E(t)$ and the charge-density wave order parameter $\mathcal{O}(t)$ after the sudden switch-on of the periodic driving. a Shows the order parameter, which was calculated with a weak pinning potential (as outlined in the Technical aspects in the Methods section) that leads to an explicit breaking of the translational symmetry. **b** Shows the difference in total energy to the initial state in units of the hopping amplitude t_h. The data in this figure was obtained from time evolution with matrix product states (MPS) for a chain length of $L = 32$ sites and both periodic (PBC) and open boundary conditions (OBC) are used.

infinite temperature state is not yet fully reached. Clearly, energy absorption is increased closer to resonance.

Driven CDW without interactions. We would like to distinguish our finding further from a known effect: In earlier works on electron-mediated CDW melting[67,68], the appearance of in-gap spectral weight was reported already in a pumped non-interacting fermion model as a genuine non-equilibrium effect. Hence, the question arises, if the in-gap band can be obtained also in a continuously driven CDW system without interactions. To study this, we adopt the "A-B model" by Shen et al.[67] at half filling,

$$\hat{H} = -t_h \sum_j \left(e^{iA(t)} c_j^\dagger c_{j+1} + \text{H.c.} \right) + \frac{U}{2} \left(\sum_{i \in A} c_i^\dagger c_i - \sum_{i \in B} c_i^\dagger c_i \right), \tag{4}$$

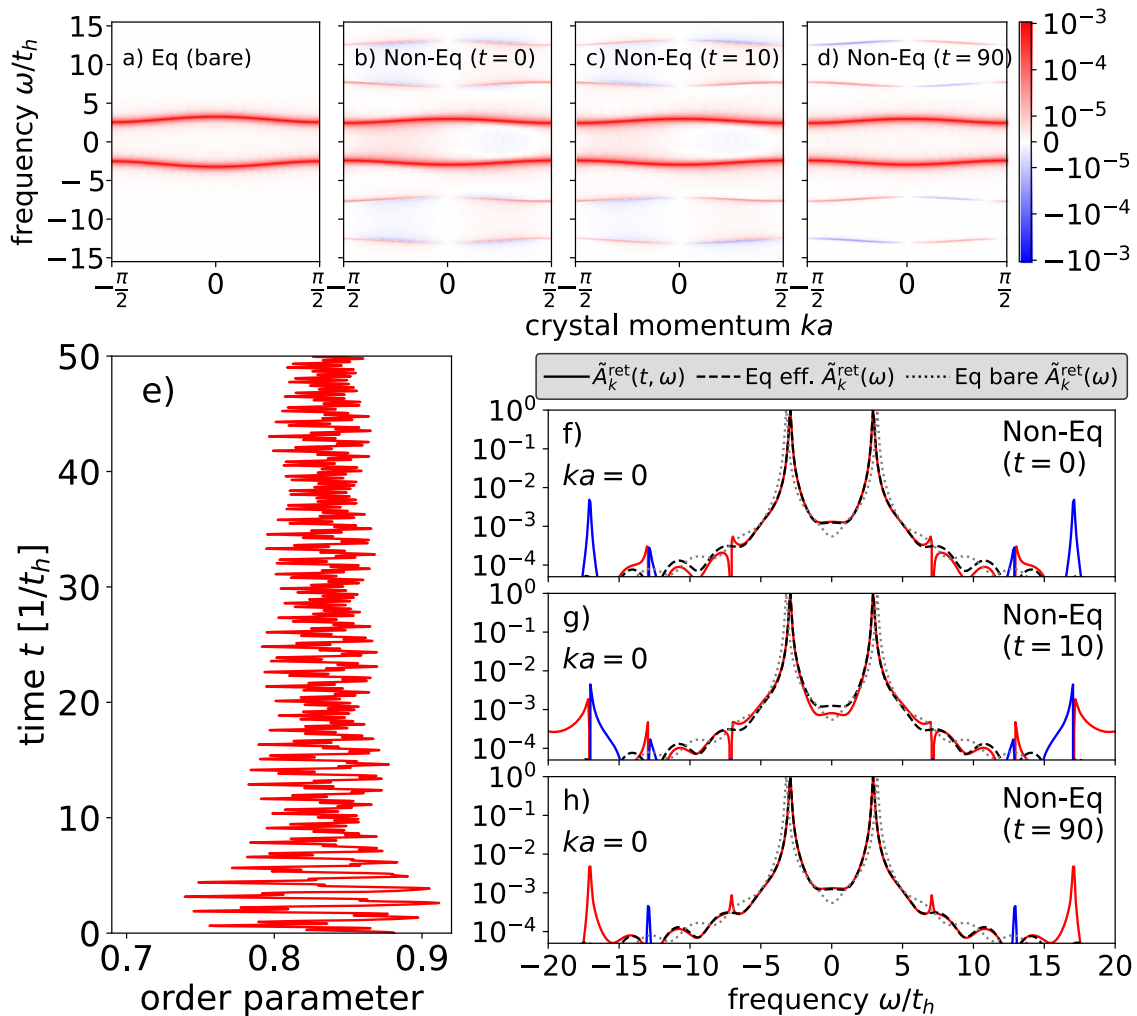and apply the same semi-infinite driving protocol used for the t-V

Fig. 5 Simulation results for the non-interacting *A-B* model (4) under semi-infinite sinusoidal driving. In this figure, an on-site potential $U = 5t_h$ and semi-infinite sinusoidal driving with amplitude $A_O = 1$ and frequency $\Omega = 10t_h$ is used. The chain length is $L = 128$ sites. The panels **a–d** show results for the non-equilibrium spectral functions $A_k^{ret}(t, \omega)$ at different times. Panel **e** shows the dynamics of the charge-density wave order parameter as a function of time and panels **f–h** show cross sections through the spectral functions of **b–d**. The color scheme encodes the values of $A_k^{ret}(t, \omega)$, where blue represents negative and red positive values.

chain. The CDW order in the model is due to the presence of a staggered on-site potential and leads to a spectral gap of size $\Delta \approx U$. We use the same Trotterized time-evolution as in the original work[67] and choose a step size of $10^{-6} t_h^{-1}$. The results of the simulations for a driving frequency of $\Omega = 10t_h$ and a gap of $U = 5t_h$ are shown in Fig. 5. Panels Fig. 5a–d show spectral functions as in Fig. 1a–d. The dynamics of the order parameter in Fig. 5e is more oscillatory than in Fig. 4a. Nevertheless, the mean value of the oscillations decreases such that one finds a reduction of the CDW order, similar to the data with $\Omega/t_h = 10$ in Fig. 4. The momentum cuts through the spectral function in Fig. 5f–h, however, show that this is not connected with the formation of a peak in the spectral gap. One should note that the spectral function does not become stationary in the model but in the in-gap region the only effect appears to be a small shift [compare Fig. 5g and h].

Mean-field dynamics. To go beyond the purely non-interacting limit we treat the dynamics of the CDW phase in the *t-V* model within a Hartree-Fock mean-field (MF) approach, whose results are shown in Fig. 6. This allows us to investigate the role of interaction-induced doublon excitations for the in-gap feature. A

more detailed discussion can be found in the Methods section. The equilibrium MF band structure is similar to the one in the *A-B* model. In the driven model, however, we obtain, in addition to the Floquet replicas of the equilibrium bands, a signal in the band gap around $\omega/t_h \approx 0$, in contrast to the findings for the non-interacting system of the previous section. This shows that an interaction-induced CDW state is essential for this feature to appear.

Comparison to finite temperatures and quench dynamics. Additional insights can be gained by comparing the results of the periodic driving to a quench to the high-frequency effective Hamiltonian as well as to finite-temperature results at equilibrium. Figure 7 displays exact diagonalization results (ED) for $A_k^{ret}(\omega)$ at finite and infinite inverse temperatures (see Methods section) β, and $A_k^{ret}(t, \omega)$ at times $t = 0$ and $t = 10$ after the quench, respectively. As can be seen in Fig. 7a and b, at low temperatures the in-gap band is not visible in the ED results, but at intermediate temperatures [$\beta = 1$, Fig. 7c] a band-like feature in the gap region becomes visible, which at $\beta = 0$ (Fig. 7d) is replaced by a flat signal around $\omega = 0$ and additional features at $\omega \sim \pm V/2$. We focus on the feature around $\omega = 0$ at intermediate
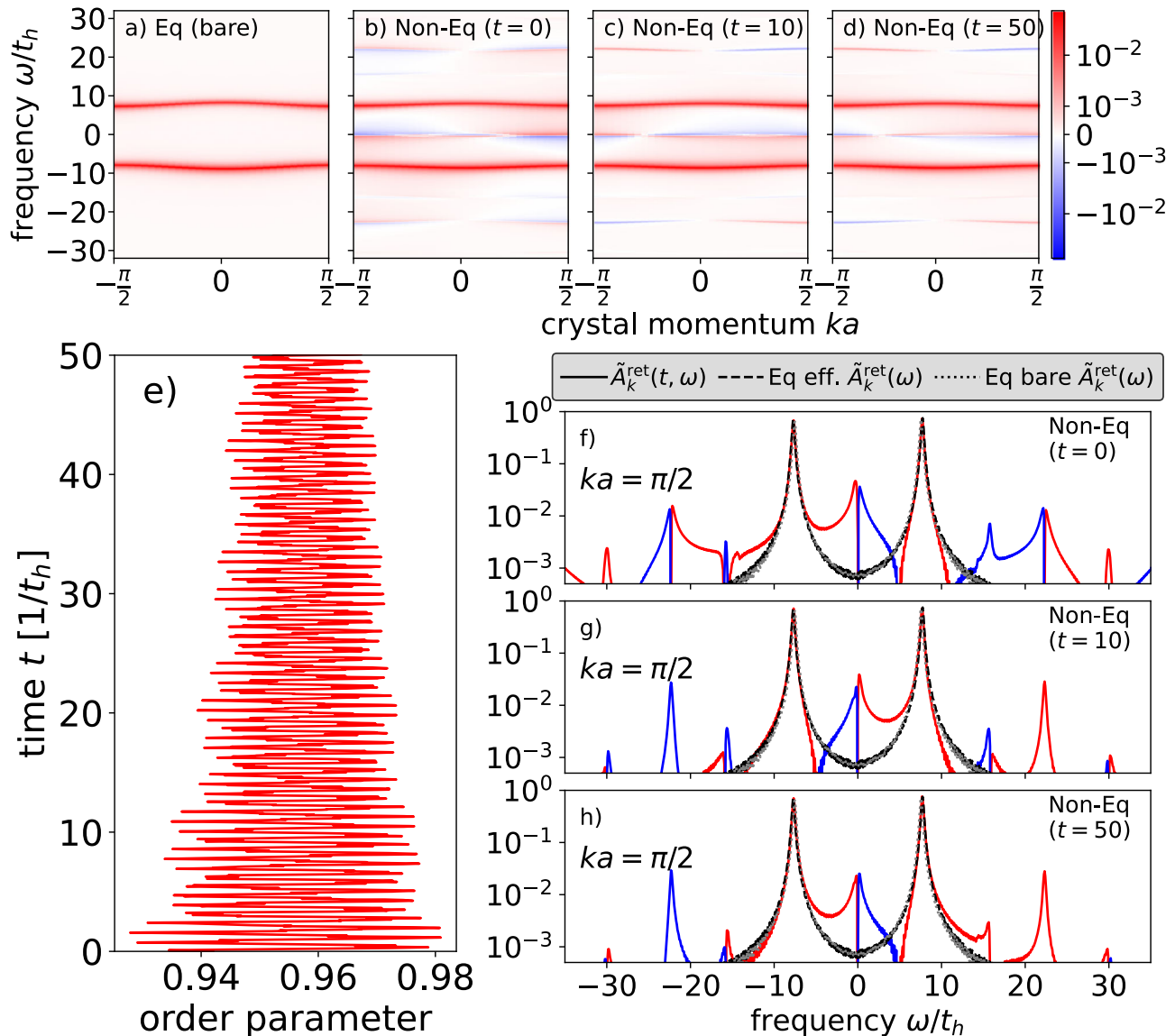
Fig. 6 Simulation results for the t-V model under semi-infinite sinusoidal driving within Hartree-Fock mean-field theory. The data in this figure was obtained for an interaction strength $V = 8t_h$ and a vector potential with amplitude $A_0 = 1$ and frequency $\Omega = 30t_h$. Panels **a**–**d** show results for the non-equilibrium spectral functions $A_k^{ret}(t, \omega)$ at different times. Panel **e** shows the dynamics of the charge-density wave order parameter as a function of time and panels **f**–**h** show cross sections through the spectral functions of **b**–**d**. The color scheme encodes the values of $A_k^{ret}(t, \omega)$, where blue represents negative and red positive values. The length of the chain is $L = 64$ sites and periodic boundary conditions have been used. The heatmaps in **a**–**d** are drawn for the reduced Brillouin zone.

temperatures, since it is most similar to the results in the periodically driven system. We checked for different values of V/t_h and find that the bandwidth and position of the in-gap band at $\beta = 1$ seems not to depend on V, similar to the driven system (cf. Supplementary Fig. 4). In the quench dynamics, already immediately after the quench a weak in-gap band is visible (Fig. 7e), which is stronger at time $t = 10$ (Fig. 7f), whose intensity, however, depends non-monotonically on time. This is in contrast to the periodically driven system, where the in-gap band seems to be a stable feature on the time scales investigated by us. These findings further support the picture that the in-gap band can be understood already in the lowest order of the high-frequency expansion. It also shows that in our case the quench dynamics contains the main spectral features of the periodically driven system.

A similar band around $\omega \sim 0$ is known to appear in the dynamical structure factor of quantum antiferromagnets, where thermal excitation leads to the formation and scattering of moving domain walls, the so-called "Villain mode", which has been observed in neutron scattering experiments[53–56]. Our findings indicate that a similar mode is obtained also in the present system at finite temperatures, and in nonequilibrium after a sudden quench or when periodically driving: In the CDW state treated here, such a domain wall is realized by a doublon, i.e. two adjacent electrons, which can freely itinerate through the system unless it recombines with the holon. The formation and delocalization of the doublon lead to a reduction of the CDW order parameter. A contribution to the spectral function stems from the scattering between populated eigenstates of the excited system with at least one doublon. Removing (adding) an electron without changing the doublon number connects two such states,
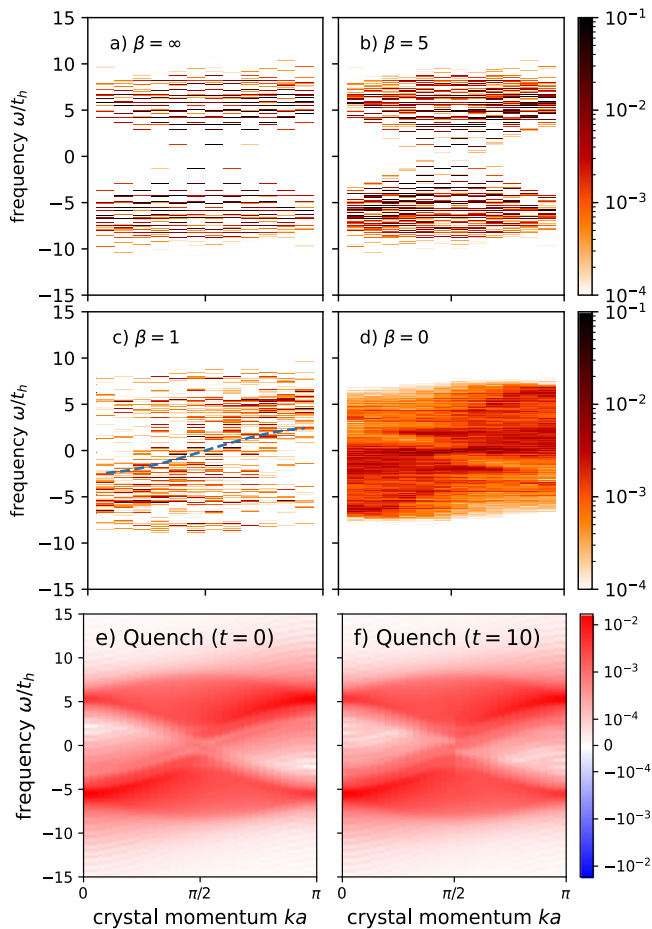
Fig. 7 Spectral functions at nonzero temperature T and after a quench.
a–d Exact diagonalization results for the equilibrium spectral function
$A_k^{\text{ret}}(\omega)$ of a chain with interaction strength $V/t_h = 5$ and inverse
temperature $\beta = 1/T$, as indicated in the panels. The dashed line in **c** is a
guide to the eye indicating the in-gap band displayed in Fig. 1d. The data
was obtained for a chain with $L = 12$ lattice sites and open boundary
conditions. **e, f** Nonequilibrium spectral function $A_k^{\text{ret}}(t, \omega)$ after a sudden
quench (no periodic driving) to the zeroth order high-frequency effective
Hamiltonian. The data is obtained from time evolution with matrix product
states in a system with $L = 32$ lattice sites for open boundary conditions.
The color scheme encodes the values of the spectral functions, where in
e and **f** blue color represents negative values.

generically at different momenta k and $k + q$. For quantum
antiferromagnets, similarly, the scattering between states formed
of a delocalized single domain wall—within the subspace of one
domain wall—leads to a sinusoidal signal around $\omega = 0$ in the
longitudinal dynamical structure factor, which then is called
the Villain mode (or resonance)[53,56,69]. This is also found for the
transversal dynamical structure factor of the XXZ
antiferromagnet[69]. The breaking of a doublon, in contrast, leads
to a signal at $\omega \sim V$, as seen in our finite-temperature results at
higher temperatures.

The MPS results show an asymmetric line-shape (see Supple-
mentary Figs. 1–3), which is also reported for the Villain mode in
antiferromagnets[69]. Although the fundamental mechanism behind
the Villain mode, i.e. free doublon propagation, can also occur in
mean-field theory, it clearly does not capture those asymmetries.
Nevertheless, our data indicates Villain-like resonances as a likely
explanation of the observed in-gap feature. To further understand
the properties of the in-gap band, a similar calculation to the one

pursued by Jones et al.[69] for the spinless-fermion model is needed,
which goes beyond the scope of this paper.

Conclusions

We report the formation of a cosine-shaped signal in the time-
dependent (retarded) spectral function upon periodic driving of
an initial CDW insulator. For driving frequencies Ω larger than
the spectral gap, it occurs in addition to the equilibrium spectral
features, which are modified according to the prediction by the
high-frequency effective Hamiltonian[29]. When approaching
resonance, the spectral function changes significantly as com-
pared to the equilibrium case and a flat band around $\omega = 0$
becomes the dominant feature.

We find these results based on quasi-exact time evolution using
matrix product states. The additional signal is not observed when
periodically driving a non-interacting CDW state, but a mean-
field treatment of the Hamiltonian (1) reveals a similar in-gap
signal around $\omega = 0$. However, its properties still differ sig-
nificantly from the MPS results, in particular with respect to the
line shape.

Comparing to finite-temperature results and to the dynamics
of a quench to the high-frequency effective Hamiltonian reveals
that also in these cases the in-gap band is present, and its
properties are very similar to the one seen in the periodically
driven system. This indicates that exciting the system by adding a
finite amount of energy populates certain states not present in the
ground state spectral function. This is reminiscent of the behavior
of the dynamical structure factor of quantum magnets, where
different possible scenarios for temperature-induced additional
branches are known, e.g., i) Villain mode of moving domain walls
in spin-1/2 quantum antiferromagnets[53–56]; ii) scattering of ele-
mentary excitations (e.g. magnons in spin-1 chains[57]); iii)
population of bound states[58]. The bandwidth of the observed in-
gap band appears to be independent of V, similar to the Villain
resonance[53], so that our fermionic system likely realizes a Villain-
like band at finite (intermediate) temperatures and out-of-equi-
librium, in both the quench dynamics and under periodic driving.
At high temperatures, a flat band is obtained at $\omega \approx 0$, which is
also observed when driving close to resonance, where the results
are very similar to the $\beta = 0$ results, indicating heating to infinite
temperature.

Note that a Villain-like mode has also been reported for the
fermionic Hubbard chain at finite temperatures, however, there it
is seen in the structure factor of the density-density
correlations[70]. It will be interesting to further investigate this
feature in this simple correlated system, e.g., using perturbative
approaches[69] or Bethe ansatz, or semiclassical approaches, such
as fermionic truncated Wigner approximations[71–73]. It is an open
question to see whether the interplay of the melting of CDW
states and electron correlations can lead to similar additional
resonances in the spectral function also in periodically driven
interacting two-dimensional systems. This is relevant for pre-
dictions for ongoing pump-probe investigations, e.g., in two-
dimensional transition metal dichalcogenides (TMDCs)[74]. It will
be fruitful to explore the interplay of such in-gap features, Floquet
side-bands and dephasing mechanisms in strongly correlated
materials, and also in related model realizations by quantum
simulators with ultracold gases on optical lattices[20,21,75].

Methods

Green's functions. All Green's functions (GFs) are derived from
the contour-ordered single-particle Green's function[76]

$$G_{\alpha\beta}(t, t') = -i\left\langle \hat{T}_C c_\alpha(t) c_\beta^\dagger(t') \right\rangle, \quad (5)$$

which can be written in a matrix representation with respect to the forward and backward branches of the real-time axis. In this representation the greater, $G^>_{\alpha\beta}(t,t')$, and lesser Green's function $G^<_{\alpha\beta}(t,t')$ each have one time argument lying on the forward and one on the backward branch of the real-time contour. The retarded GF is a linear combination of the two with an additional theta function,

$$
\begin{aligned}
G^{\mathrm{ret}}_{\alpha\beta}(t,t') &= \theta(t-t')\Big(G^>_{\alpha\beta}(t,t') - G^<_{\alpha\beta}(t,t')\Big)\\
&:= -i\theta(t-t')\Big(\big\langle c_\alpha(t)c^\dagger_\beta(t')\big\rangle + \big\langle c^\dagger_\beta(t')c_\alpha(t)\big\rangle\Big).
\end{aligned}
\tag{6}
$$

At equilibrium, one of the two time variables can be suppressed due to time-translational invariance. Out-of-equilibrium, however, one needs to consider both time variables, and the Fourier transform to frequency space is not unique any more. In order to minimize the numerical costs, we choose to use "horizontal" time coordinates, in which we evolve the wavefunction up to a time t' and then perform the Fourier transform with respect to the relative time $\tau = t - t'$, after further evolving the system in time, with $t > t'$. Kalthoff et al.[37] obtained similar results for this choice of the waiting time and the Wigner choice $(t+t')/2$ in the case of a free fermion model. The states are labelled by momentum indices k (depending on boundary conditions, see below). In the numerics we calculate the auxiliary quantities

$$
\begin{aligned}
C^<_{kl}(t',\tau) &= \langle c^\dagger_k(t'+\tau)c_l(t')\rangle\\
C^>_{kl}(t',\tau) &= \langle c_l(t')c^\dagger_k(t'+\tau)\rangle,
\end{aligned}
\tag{7}
$$

such that

$$
G^{\mathrm{ret},\lessgtr}_{kk}(t',\tau) = -i\theta(\tau)C^{\lessgtr}_{kk}(t',\tau)^*,
\tag{8}
$$

and we finally obtain the nonequilibrium spectral functions

$$
\begin{aligned}
A^{\mathrm{ret},\lessgtr}_k(t,\omega) &= -\mathrm{Im}\,\frac{1}{\sqrt{2\pi}}\int_{-\infty}^{\infty}\mathrm{d}\tau\,e^{(i\omega-\eta)\tau}G^{\mathrm{ret},\lessgtr}_{kk}(t,\tau),\\
A^{\mathrm{ret}}_k(t,\omega) &= A^{\mathrm{ret},<}_k(t,\omega) + A^{\mathrm{ret},>}_k(t,\omega).
\end{aligned}
\tag{9}
$$

In equilibrium the retarded GF contains information about the density of states while the lesser and greater GFs contain information about occupations of the states. The latter is reflected in the fact that due to the absence of the $\theta(\tau)$ the whole "history" of the lesser and greater GFs needs to be traced back until time $-\infty$. In this work we only compute the retarded Green's function. Integration of $A^{\mathrm{ret}}_k(t,\omega)$ over k directly yields the time-dependent local density of states. In contrast to the equilibrium situation the quantity $A^{\mathrm{ret}}_k(t,\omega)$ is not necessarily positive, so that care needs to be taken with this interpretation[63].

A more subtle issue concerns the gauge-invariance of the calculated spectral function. In accordance with other studies in the literature[44,77], we perform calculations in a fixed gauge. Gauge-invariant formulations have been proposed[17,61,62], in particular for overlapping pump and probe pulses, or if the system possesses multiple bands. These are, however, difficult to implement in practice and fixed-gauge calculations already yield qualitatively insightful results.

Therefore, we focus on the most important qualitative features evolving with time. Central predictions of Floquet theory, like the effective Hamiltonian picture, are captured with a good accuracy, so that we believe that our results not only provide a qualitative picture, but also quantitative predictions with a good accuracy.

Technical aspects
Spatial Fourier transform. For periodic boundary conditions (PBC) we use $k \in \frac{2\pi}{L}\cdot\{0,\ldots,L\}$ while for open boundary conditions (OBC) $k \in \frac{\pi}{L+1}\cdot\{1,\ldots,L\}$ corresponding to a sine

transform[78,79] with

$$
c_k = \sqrt{\frac{2}{L+1}}\sum_k \sin(kr_i)c_i.
\tag{10}
$$

The OBC momenta differ slightly ($\sim 1/(L+1)$) from simple fractions of π, e.g. $\pi/2$, so we always write $\approx$ and the closest k-value.

Temporal Fourier transform. Due to the finite maximal τ that we are able to reach and due to the theta function, the temporal Fourier transform produces a non-zero background $\sim 10^{-5}$ signal everywhere in the spectral function. Since we expect the exact spectral function to have value zero if no signal is present, we decided to subtract this background. We add a damping factor $\eta \approx 0.1$ to regularize the finite time-propagation with respect to τ. In addition, to improve the ω-resolution we padded the τ-data with zeros to obtain at least 4096 frequency points.

Symmetry-broken CDW state. For MPS calculations with OBCs we prepare the system at half filling with $\mu_l = 0$. In the CDW phase, this leads to an exact superposition of the two possible symmetry-broken ground states, so that for a finite system $\mathcal{O}_{\mathrm{CDW}}(t) = 0$ for all times t. In order to be able to keep track of the dynamics of the CDW order parameter, we performed additional simulations where we applied a 'pinning field' at the edge $\mu_{1,L} \neq 0$, which selects one of the ground states and allows us to study $\mathcal{O}_{\mathrm{CDW}}(t)$. We checked that the spectral function does not differ if calculated with or without the pinning field. In order to minimize possible boundary effects in the order parameter, we perform the sum in Eq. (3) only over the four unit cells in the center of the system.

MPS calculations. For comprehensive reviews we refer to the literature[48,49]. Here we only focus on the main aspects concerning the computation of the time-dependent spectral functions. In order to compute $G^{\mathrm{ret},\lessgtr}_{kk}(t,\tau)$ using matrix product states we start from the system's ground state $|\mathrm{GS}\rangle$ and consider the following quantum states

$$
\begin{aligned}
|\psi(t)\rangle &= U_{\mathrm{TDVP}}(t,0)|\mathrm{GS}\rangle,\\
|\phi^<_l(t)\rangle &= c_l|\psi(t)\rangle,\\
|\phi^>_l(t)\rangle &= c^\dagger_l|\psi(t)\rangle,\\
|\phi^{\lessgtr}_l(t+\tau)\rangle &= U_{\mathrm{TDVP}}(t+\tau,t)|\phi^{\lessgtr}_l(t)\rangle,
\end{aligned}
\tag{11}
$$

where $U_{\mathrm{TDVP}}(t,t_0)$ denotes time-evolution using the MPS realization of the time-dependent variational principle (TDVP). Here, we always apply a two-site TDVP algorithm[49]. The operators c_k carry momentum space labels. However, we always work in position space and exploit that we can write momentum space annihilation and creation operators as a sum of local operators $c_k = \sum_j P_{k,j}c_j$, where we have introduced the transformation matrix P, allowing us to compute $C^{\lessgtr}_{kl}(t,\tau)$ through a series of local MPO-MPS applications. P depends on the boundary conditions used. Using the states (11) we calculate the quantities

$$
C^<_{kl}(t,\tau) = \Big\langle \psi(t+\tau)|c^\dagger_k|\phi^<_l(t+\tau)\Big\rangle,
\tag{12}
$$

$$
C^>_{kl}(t,\tau) = \Big\langle \phi^>_l(t+\tau)|c^\dagger_k|\psi(t+\tau)\Big\rangle,
\tag{13}
$$

which are related to $G^{\mathrm{ret},\lessgtr}_{kk}(t,\tau)$, see Eq. (8). For PBC we implement a "snake geometry" (Paeckel, S. & Köhler, T. Private communication)[80] for the labelling of the sites in the chain. It turned out that the DMRG ground state search always choses one of the degenerate ground states which allowed us to calculate the order parameter directly. Further details on the calculation of the

non-equilibrium spectral function with MPS methods can be found elsewhere[79].

Hartree-Fock time evolution. We start from a Hartree-Fock decoupling of the interaction term and assume a two-site unit cell with sublattices A and B. Let us denote

$$\rho_A := \langle c_i^\dagger c_i \rangle_{i \in A}, \quad \rho_0 := \langle c_i^\dagger c_{i+1} \rangle_{i \in A},$$
$$\rho_B := \langle c_i^\dagger c_i \rangle_{i \in B}, \quad \rho_1 := \langle c_i^\dagger c_{i+1} \rangle_{i \in B}. \tag{14}$$

Using the Fourier basis ($Q = \pi$)

$$c_{i \in A}^\dagger = \frac{1}{\sqrt{V}} \sum_{k \in \text{rBZ}} e^{-ikr_i} \left(c_k^\dagger + c_{k+Q}^\dagger \right)$$
$$c_{i \in B}^\dagger = \frac{1}{\sqrt{V}} \sum_{k \in \text{rBZ}} e^{-ikr_i} \left(c_k^\dagger - c_{k+Q}^\dagger \right) \tag{15}$$

we obtain, using the definitions $\epsilon_k = -2t_h \cos(k)$, $\chi_k = V(\rho_0 e^{-ik} + \rho_1^* e^{ik})$, the following representation of the Hamiltonian

$$(H) = \begin{pmatrix} c_k^\dagger & c_{k+Q}^\dagger \end{pmatrix}$$
$$\begin{pmatrix} \epsilon_k - \text{Re}(\chi_k) + V(\rho_A + \rho_B) - \mu & i\text{Im}(\chi_k) + V(\rho_B - \rho_A) \\ -i\text{Im}(\chi_k) + V(\rho_B - \rho_A) & -\epsilon_k + \text{Re}(\chi_k) + V(\rho_A + \rho_B) - \mu \end{pmatrix}$$
$$\begin{pmatrix} c_k \\ c_{k+Q} \end{pmatrix}. \tag{16}$$

In the following we consider half filling $\mu = V(\rho_A + \rho_B)$. The saddle point values of ρ_A, ρ_B, etc. are determined with a simulated annealing approach. Diagonalization of the Hamiltonian yields the eigenenergies

$$E_k = \pm \left\{ -\left[-\left(\epsilon_k - \text{Re}(\chi_k)\right)^2 - \text{Im}(\chi_k)^2 - V^2(\rho_B - \rho_A)^2 \right] \right\}^{1/2}$$
$$= \pm \left\{ |\epsilon_k - \chi_k|^2 + V^2(\rho_B - \rho_A)^2 \right\}^{1/2}. \tag{17}$$

Hence, the spectral gap is given by $2V(\rho_B - \rho_A)$.

For the dynamics we first solve the time-diagonal problem and obtain the full one-particle reduced density matrix $\rho_{ij}(t) = \langle c_i^\dagger(t) c_j(t) \rangle$. In a second iteration we solve the equation of motion for the relative time τ using the time-diagonal data from the first iteration. This corresponds to solving the Kadanoff-Baym equations with a Hartree-Fock self-energy[76].

Computation of the finite-temperature spectral function. We use the Lehmann representation for the equilibrium retarded spectral function at finite temperatures,

$$A_k^{\text{ret}}(\omega) = \frac{1}{Z} \sum_{m,n} |\langle m | c_k | n \rangle|^2 \left(e^{-\beta E_n} + e^{-\beta E_m} \right) \cdot$$
$$\delta\left((E_n - E_m) - \omega \right), \tag{18}$$

where $Z = \sum_n e^{-\beta E_n}$ is the partition function. The eigenstates $|m\rangle$ and $|n\rangle$ as well as the eigenvalues E_n of the Hamiltonian (1) evaluated at time $t = 0$ were obtained using QuSpin[81,82]. We grouped the frequencies into bins of width 10^{-2}.

Data availability

All data shown in this paper (MPS, noninteracting, mean-field and exact diagonalization calculations) can be accessed at the repository https://gitlab.gwdg.de/stefan-kehrein-condensed-matter-theory/alexander-osterkorn/cdw_chain_dynamics.

Code availability

The matrix product state calculations have been carried out using the SymMPS toolkit (developed by Sebastian Paeckel and Thomas Köhler), which is freely available at www.symmps.eu (accessed on 2020-09-23). The exact diagonalization results at nonzero temperature in Fig. 7 were obtained using QuSpin[81,82], which is available at quspin.github.io/QuSpin (version 0.3.7). The codes for the noninteracting A-B and for the mean-field time evolution are available in the same repository as the data (see "Data Availability"). Further configuration files and scripts can be obtained from the authors upon request.

References

1. Mitrano, M. et al. Possible light-induced superconductivity in k3c60 at high temperature. *Nature* **530**, 461–464 (2016).
2. Fausti, D. et al. Light-induced superconductivity in a stripe-ordered cuprate. *Science* **331**, 189–191 (2011).
3. Hu, W. et al. Optically enhanced coherent transport in yba2cu3o6.5 by ultrafast redistribution of interlayer coupling. *Nat. Mater.* **13**, 705–711 (2014).
4. Wang, Y., Chen, C.-C., Moritz, B. & Devereaux, T. P. Light-enhanced spin fluctuations and d-wave superconductivity at a phase boundary. *Phys. Rev. Lett.* **120**, 246402 (2018).
5. Paeckel, S. et al. Detecting superconductivity out of equilibrium. *Phys. Rev. B* **101**, 180507 (2020).
6. Erben, D. et al. Excitation-induced transition to indirect band gaps in atomically thin transition-metal dichalcogenide semiconductors. *Phys. Rev. B* **98**, 035434 (2018).
7. Jin, C. et al. Ultrafast dynamics in van der waals heterostructures. *Nat. Nanotechnol.* **13**, 994–1003 (2018).
8. Zhu, H. et al. Interfacial charge transfer circumventing momentum mismatch at two-dimensional van der waals heterojunctions. *Nano Lett.* **17**, 3591–3598 (2017).
9. Kunstmann, J. et al. Momentum-space indirect interlayer excitons in transition-metal dichalcogenide van der waals heterostructures. *Nat. Phys.* **14**, 801–805 (2018).
10. Jin, C. et al. Observation of moiré excitons in wse2/ws2 heterostructure superlattices. *Nature* **567**, 76–80 (2019).
11. Chernikov, A., Ruppert, C., Hill, H. M., Rigosi, A. F. & Heinz, T. F. Population inversion and giant bandgap renormalization in atomically thin ws2 layers. *Nat. Photonics* **9**, 466–470 (2015).
12. Hellmann, S. et al. Time-domain classification of charge-density-wave insulators. *Nat. Commun.* **3**, 1069 (2012).
13. de la Torre, A. et al. Colloquium: Nonthermal pathways to ultrafast control in quantum materials. *Revi. Mod. Phys.* **93**, 041002 (2021).
14. Oka, T. & Kitamura, S. Floquet engineering of quantum materials. *Annu. Rev. Condens. Matter Phys.* **10**, 387–408 (2019).
15. Kennes, D. M. & Rubio, A. A new era of quantum materials mastery and quantum simulators in and out of equilibrium https://arxiv.org/abs/2204.11928 (2022).
16. Krausz, F. & Ivanov, M. Attosecond physics. *Rev. Mod. Phys.* **81**, 163–234 (2009).
17. Freericks, J. K., Krishnamurthy, H. R., Ge, Y., Liu, A. Y. & Pruschke, T. Theoretical description of time-resolved pump/probe photoemission in TaS2: A single-band DFT+DMFT(NRG) study within the quasiequilibrium approximation. *Phys. Stat. Solidi (b)* **246**, 948–954 (2009).
18. Golež, D., Werner, P. & Eckstein, M. Photoinduced gap closure in an excitonic insulator. *Phys. Rev. B* **94**, 035121 (2016).
19. Ejima, S., Lange, F. & Fehske, H. Photoinduced metallization of excitonic insulators. *Phys. Rev. B* **105**, 245126 (2022).
20. Bloch, I., Dalibard, J. & Zwerger, W. Many-body physics with ultracold gases. *Rev. Mod. Phys.* **80**, 885–964 (2008).
21. Bloch, I. Ultracold quantum gases in optical lattices. *Nat. Phys.* **1**, 23–30 (2005).
22. Bloch, I., Dalibard, J. & Nascimbène, S. Quantum simulations with ultracold quantum gases. *Nat. Phys.* **8**, 267–276 (2012).
23. Aidelsburger, M. et al. Experimental realization of strong effective magnetic fields in an optical lattice. *Phys. Rev. Lett.* **107**, 255301 (2011).
24. Aidelsburger, M. et al. Experimental realization of strong effective magnetic fields in optical superlattice potentials. *Appl. Phys. B* **113**, 1–11 (2013).
25. Schweizer, C., Lohse, M., Citro, R. & Bloch, I. Spin pumping and measurement of spin currents in optical superlattices. *Phys. Rev. Lett.* **117**, 170405 (2016).
26. Trotzky, S. et al. Time-resolved observation and control of superexchange interactions with ultracold atoms in optical lattices. *Science* **319**, 295–299 (2008).

27. Bukov, M., D'Alessio, L. & Polkovnikov, A. Universal high-frequency behavior of periodically driven systems: From dynamical stabilization to Floquet engineering. *Adv. Phys.* **64**, 139–226 (2015).

28. Eckardt, A. Colloquium: Atomic quantum gases in periodically driven optical lattices. *Rev. Mod. Phys.* **89**, 011004 (2017).

29. Kennes, D. M., de la Torre, A., Ron, A., Hsieh, D. & Millis, A. J. Floquet Engineering in Quantum Chains. *Phys. Rev. Lett.* **120**, 127601 (2018).

30. Kitagawa, T., Berg, E., Rudner, M. & Demler, E. Topological characterization of periodically driven quantum systems. *Phys. Rev. B* **82**, 235114 (2010).

31. Vogl, M., Rodriguez-Vega, M. & Fiete, G. A. Effective Floquet Hamiltonian in the low-frequency regime. *Phys. Rev. B* **101**, 024303 (2020).

32. Eckardt, A. & Anisimovas, E. High-frequency approximation for periodically driven quantum systems from a Floquet-space perspective. *New J. Phys.* **17**, 093039 (2015).

33. Vogl, M., Laurell, P., Barr, A. D. & Fiete, G. A. Flow Equation Approach to Periodically Driven Quantum Systems. *Phys. Rev. X* **9**, 021037 (2019).

34. Lazarides, A., Das, A. & Moessner, R. Equilibrium states of generic quantum systems subject to periodic driving. *Phys. Rev. E* **90**, 012110 (2014).

35. D'Alessio, L. & Rigol, M. Long-time behavior of isolated periodically driven interacting lattice systems. *Phys. Rev. X* **4**, 041048 (2014).

36. Kuwahara, T., Mori, T. & Saito, K. Floquet–magnus theory and generic transient dynamics in periodically driven many-body quantum systems. *Ann. Phys.* **367**, 96–124 (2016).

37. Kalthoff, M. H., Uhrig, G. S. & Freericks, J. K. Emergence of Floquet behavior for lattice fermions driven by light pulses. *Phys. Rev. B* **98**, 035138 (2018).

38. Novičenko, V., Anisimovas, E. & Juzeliūnas, G. Floquet analysis of a quantum system with modulated periodic driving. *Phys. Rev. A* **95**, 023615 (2017).

39. Novičenko, V., Žlabys, G. & Anisimovas, E. Flow-equation approach to quantum systems driven by an amplitude-modulated time-periodic force. *Phys. Rev. A* **105**, 012203 (2022).

40. Herrmann, A., Murakami, Y., Eckstein, M. & Werner, P. Floquet prethermalization in the resonantly driven Hubbard model. *EPL* **120**, 57001 (2017).

41. Bukov, M., Kolodrubetz, M. & Polkovnikov, A. Schrieffer-Wolff Transformation for Periodically Driven Systems: Strongly Correlated Systems with Artificial Gauge Fields. *Phys. Rev. Lett.* **116**, 125301 (2016).

42. Wang, Y. H., Steinberg, H., Jarillo-Herrero, P. & Gedik, N. Observation of Floquet-Bloch States on the Surface of a Topological Insulator. *Science* **342**, 453–457 (2013).

43. Mahmood, F. et al. Selective scattering between floquet–bloch and volkov states in a topological insulator. *Nat. Phys.* **12**, 306–310 (2016).

44. Schüler, M. et al. How circular dichroism in time- and angle-resolved photoemission can be used to spectroscopically detect transient topological states in graphene. *Phys. Rev. X* **10**, 041013 (2020).

45. Sato, S. A. et al. Floquet states in dissipative open quantum systems. *J. Phys. B* **53**, 225601 (2020).

46. Aeschlimann, S. et al. Survival of floquet-bloch states in the presence of scattering. *Nano Lett.* **21**, 5028–5035 (2021). PMID: 34082532.

47. Bittner, N., Golež, D., Eckstein, M. & Werner, P. Photoenhanced excitonic correlations in a mott insulator with nonlocal interactions. *Phys. Rev. B* **101**, 085127 (2020).

48. Schollwöck, U. The density-matrix renormalization group in the age of matrix product states. *Ann. Phys.* **326**, 96–192 (2011).

49. Paeckel, S. et al. Time-evolution methods for matrix-product states. *Ann. Phys.* **411**, 167998 (2019).

50. Sachdev, S. Quantum phase transitions. *Phys. World* **12**, 33 (1999).

51. Giamarchi, T. *Quantum Physics in One Dimension* (Oxford University Press, 2003).

52. Gebhard, F. *The Mott Metal-Insulator Transition: Models and Methods.* Springer Tracts in Modern Physics (Springer Berlin Heidelberg, Berlin Heidelberg, https://books.google.de/books?id=uCPgHgEKnwEC 1997).

53. Villain, J. Propagative spin relaxation in the ising-like antiferromagnetic linear chain. *Physica B+C* **79**, 1–12 (1975).

54. Yoshizawa, H., Hirakawa, K., Satija, S. K. & Shirane, G. Dynamical correlation functions in a one-dimensional ising-like antiferromagnetic cscocl$_3$: A neutron scattering study. *Phys. Rev. B* **23**, 2298–2307 (1981).

55. Nagler, S. E., Buyers, W. J. L., Armstrong, R. L. & Briat, B. Propagating domain walls in cscobr$_3$. *Phys. Rev. Lett.* **49**, 590–592 (1982).

56. Bera, A. K. et al. Spinon confinement in a quasi-one-dimensional anisotropic heisenberg magnet. *Phys. Rev. B* **96**, 054423 (2017).

57. Becker, J. et al. Finite-temperature dynamics and thermal intraband magnon scattering in haldane spin-one chains. *Phys. Rev. B* **96**, 060403 (2017).

58. Nayak, M. & Mila, F. Possibility to detect the bound state of the heisenberg ferromagnetic chain at intermediate temperature. *Phys. Rev. B* **105**, 094407 (2022).

59. Peierls, R. Zur Theorie des Diamagnetismus von Leitungselektronen. *Z. Physik* **80**, 763–791 (1933).

60. Des Cloizeaux, J. & Gaudin, M. Anisotropic Linear Magnetic Chain. *J. Math. Phys.* **7**, 1384–1400 (1966).

61. Freericks, J. K., Krishnamurthy, H. R., Sentef, M. A. & Devereaux, T. P. Gauge invariance in the theoretical description of time-resolved angle-resolved pump/probe photoemission spectroscopy. *Phys. Scr.* **T165**, 014012 (2015).

62. Freericks, J. K. & Krishnamurthy, H. R. Constant Matrix Element Approximation to Time-Resolved Angle-Resolved Photoemission Spectroscopy. *Photonics* **3**, 58 (2016).

63. Kalthoff, M. H., Kennes, D. M. & Sentef, M. A. Floquet-engineered light-cone spreading of correlations in a driven quantum chain. *Phys. Rev. B* **100**, 165125 (2019).

64. Dunlap, D. & Kenkre, V. Dynamic localization of a charged particle moving under the influence of an electric field. *Phys. Rev. B* **34**, 3625 (1986).

65. Pereira, R. G., White, S. R. & Affleck, I. Spectral function of spinless fermions on a one-dimensional lattice. *Phys. Rev. B* **79**, 165113 (2009).

66. Uhrig, G. S., Kalthoff, M. H. & Freericks, J. K. Positivity of the Spectral Densities of Retarded Floquet Green Functions. *Phys. Rev. Lett.* **122**, 130604 (2019).

67. Shen, W., Devereaux, T. P. & Freericks, J. K. Exact solution for Bloch oscillations of a simple charge-density-wave insulator. *Phys. Rev. B* **89**, 235129 (2014).

68. Shen, W. et al. Nonequilibrium "Melting" of a Charge Density Wave Insulator via an Ultrafast Laser Pulse. *Phys. Rev. Lett.* **112**, 176404 (2014).

69. James, A. J. A., Goetze, W. D. & Essler, F. H. L. Finite-temperature dynamical structure factor of the heisenberg-ising chain. *Phys. Rev. B* **79**, 214408 (2009).

70. Nocera, A., Essler, F. H. L. & Feiguin, A. E. Finite-temperature dynamics of the mott insulating hubbard chain. *Phys. Rev. B* **97**, 045146 (2018).

71. Davidson, S. M., Sels, D. & Polkovnikov, A. Semiclassical approach to dynamics of interacting fermions. *Ann. Phys.* **384**, 128–141 (2017).

72. Osterkorn, A. & Kehrein, S. Systematic large flavor fTWA approach to interaction quenches in the Hubbard model. *arXiv:2007.05063* [*cond-mat, physics:quant-ph*] (2020). 2007.05063.

73. Osterkorn, A. & Kehrein, S. Photoinduced prethermal order parameter dynamics in the two-dimensional large-n hubbard-heisenberg model. *Phys. Rev. B* **106**, 214318 (2022).

74. Manzeli, S., Ovchinnikov, D., Pasquier, D., Yazyev, O. V. & Kis, A. 2d transition metal dichalcogenides. *Nat. Rev. Mater.* **2**, 17033 (2017).

75. Greiner, M. & Fölling, S. Optical lattices. *Nature* **453**, 736–738 (2008).

76. Stefanucci, G. & Van Leeuwen, R. *Nonequilibrium many-body theory of quantum systems: a modern introduction* (Cambridge University Press, 2013).

77. Sentef, M. A. et al. Theory of Floquet band formation and local pseudospin textures in pump-probe photoemission of graphene. *Nat. Commun.* **6**, 1–8 (2015).

78. Köhler, T., Paeckel, S., Meyer, C. & Manmana, S. R. Formation of spatial patterns by spin-selective excitations of interacting fermions. *Phys. Rev. B* **102**, 235166 (2020).

79. Meyer, C. & Manmana, S. R. Formation of spinful dark excitons in Hubbard systems with magnetic superstructures. *arXiv:2109.07037* [*cond-mat*] (2021). 2109.07037.

80. Wilke, R. H., Köhler, T., Palm, F. A. et al. Symmetry-protected Bose-Einstein condensation of interacting hardcore bosons. *Commun Phys* **6**, 182 https://doi.org/10.1038/s42005-023-01303-z (2023).

81. Weinberg, P. & Bukov, M. QuSpin: a Python package for dynamics and exact diagonalisation of quantum many body systems part I: spin chains. *SciPost Phys.* **2**, 003 (2017).

82. Weinberg, P. & Bukov, M. QuSpin: a Python package for dynamics and exact diagonalisation of quantum many body systems. Part II: bosons, fermions and higher spins. *SciPost Phys.* **7**, 020 (2019).

Acknowledgements

Author contributions

A.O. performed the *A-B* model, mean-field and ED calculations. C.M. performed the MPS numerics. Both worked on the figures. All authors analyzed the data and discussed the results. A.O. and S.R.M. wrote and revised the manuscript with input from C.M.

Competing interests
The authors declare no competing interests.

Additional information
Supplementary information The online version contains supplementary material available at https://doi.org/10.1038/s42005-023-01346-2.

Correspondence and requests for materials should be addressed to Alexander Osterkorn or Salvatore R. Manmana.

Peer review information *Communications Physics* thanks the anonymous reviewers for their contribution to the peer review of this work. A peer review file is available.

Reprints and permission information is available at http://www.nature.com/reprints

Publisher's note Springer Nature remains neutral with regard to jurisdictional claims in published maps and institutional affiliations.